

## Dynamics of a thin film driven by a moving pressure source

D. Lunz\* and P. D. Howell

*Mathematical Institute, University of Oxford, Oxford OX2 6GG, United Kingdom*



(Received 31 May 2018; published 6 November 2018)

Motivated by the liquid metal coating on a divertor in a tokamak, we investigate the flow of a thin film of incompressible fluid on an inclined substrate subjected to a localized external pressure that oscillates parallel to the substrate. When the movement of the pressure occurs on a timescale significantly longer than the characteristic time for the thin film to equilibrate, the system is quasisteady. In the opposite extreme, where the pressure oscillates much faster than the response time of the free surface, a multiple-scale analysis shows that the free surface is exposed to an effective time-averaged pressure profile. Thus the oscillations can act to spread the momentum load of the applied pressure, resulting in smaller deformations of the liquid film. In the intermediate case, where the intrinsic and external timescales are similar, we find that there exists a critical speed of oscillations which maximizes the free-surface deflection and results in a possibly dangerous thinning of the film. Further local maxima in the free-surface deflection are caused by a fascinating nonlocal wave interaction mechanism.

DOI: [10.1103/PhysRevFluids.3.114801](https://doi.org/10.1103/PhysRevFluids.3.114801)

### I. INTRODUCTION

Thin films of fluid are ubiquitous in both the natural world and industrial processes, and have been studied extensively [1–3]. One industrial application of interest is the use of a thin film of liquid metal to coat components within a tokamak, the vessel used to magnetically confine a plasma [4]. Matter produced from fusion reactions within a tokamak, as well as any impurities that find their way to the plasma, is exhausted from the confined region and directed towards a component known as the divertor. Due to the extreme heat load of the impacting plasma, a solid surface can suffer severe surface damage, making its long-term use infeasible. One promising solution is to maintain a constantly recycled thin film of liquid metal (typically lithium) to cover and protect the solid substrate (see [5] and references therein).

The hot ions impacting the divertor impart mass, momentum, and thermal energy to the free surface of the liquid film. The contribution of the mass is negligible [6] and will be ignored in this paper. The transfer of thermal energy may be significant, but will be similarly neglected in this paper in order to focus on the isothermal, purely hydrodynamical effect of the transfer of momentum. The ions penetrate only the top surface of the thin film [7] and thus the transfer of momentum can be adequately modeled as a pressure applied to the free surface. Moreover, the strike point, the location at which the plasma exhaust is directed to impact the divertor, is controllable within the tokamak. Of particular interest is the case when the strike point is oscillated, so as to spread the heat load. To protect the solid substrate along the extent of the divertor, we must ensure that the liquid does not thin or dry out due to the applied pressure. This requirement leads us to the focus of this paper: What is the effect of a moving localized pressure applied to the free surface of a thin film of flowing fluid?

---

\*Corresponding author: [davin.lunz@maths.ox.ac.uk](mailto:davin.lunz@maths.ox.ac.uk)

Previous work on the dynamics at the liquid-metal–plasma interface has focused on Kelvin-Helmholtz [8], Rayleigh-Taylor [9], Rayleigh-Plateau [10], and electrohydrodynamic instabilities [11], as well as boiling-induced droplet ejection [12]. Our approach is to model the liquid metal as a thin film, using lubrication theory and incorporating electrodynamic effects through a Lorentz body force.

In much of the previous work on thin films, the gas above the viscous liquid film was modeled as a passive atmosphere at constant pressure. However, our model must include a pressure source that varies in both space and time. Such a pressure term has been modeled previously in situations in which an external flow has a significant effect on the behavior of the fluid film, such as jet stripping and blade coating processes (see [13–15] and references therein). Applications in microfluidics have used Marangoni forcing to achieve strikingly similar results [16]. These previous studies focused primarily on pressure profiles that either are fixed or move at constant speed and on corresponding steady or traveling-wave solutions for the thin-film response, when they exist. In this work we instead consider fully time-dependent flow caused by an oscillating pressure profile. This approach allows us to extend previous studies to find solutions in regions of parameter space where steady or traveling-wave solutions do not exist.

We find that this problem contains two characteristic timescales: the timescale corresponding to the motion of the pressure and the response timescale of the free surface. Thus the problem is naturally separated into three regimes. When the timescale associated with the motion of the pressure is much longer than the free-surface deformation timescale, the system is quasisteady: The free surface adopts its steady-state profile and varies only parametrically with the location of the applied pressure. At the other extreme, when the pressure oscillates much faster than the time for the free surface to deform, a multiple-scale analysis shows that the free surface evolves under the influence of an effective pressure, given by the average pressure over one period of its oscillation. This means that the momentum load is spread across the sweeping range (along with the heat load), and the resulting deflections in the free surface are correspondingly smaller.

Finally, when the two timescales in the problem are of similar magnitude, a direct numerical simulation reveals that the deflections can become much larger than in the two extreme cases described above. We explore the causes of this resonance and find that there are two mechanisms leading to the increased deflection magnitude. The dominant mechanism comes into play when the applied pressure sweeps at a speed close to the downstream wave propagation speed. In this case, the pressure propagates at a similar speed to the trough that it has created, thus magnifying its thinning influence. An unexpected secondary effect that also leads to a local maximum in the free-surface deflection is a nonlocal wave interaction, whereby a trough generated upstream coincides on its propagation downstream with a trough being generated later in the oscillation cycle.

We emphasize that, despite the inspiration for this study, and the numerical results presented here, stemming from a magnetohydrodynamic flow, the phenomena described are essentially hydrodynamic. Therefore, the results presented below would be qualitatively preserved in other flow regimes, including magnetohydrodynamic flows with different field orientations and classical hydrodynamic flows.

The paper is organized as follows. In Sec. II we outline the thin-film equation to be studied. In Secs. III–V we explore the three regimes of low-, high-, and moderate-frequency sweeping, respectively. In Sec. VI we summarize our findings.

## II. THIN-FILM MODEL WITH MOVING PRESSURE SOURCE

We consider the two-dimensional flow of a film of incompressible fluid on a plate inclined at an angle  $\theta$  to the horizontal, as illustrated in Fig. 1. Provided the aspect ratio of the characteristic height to the characteristic length of the fluid film is small, the lubrication approximation can be applied to reduce the governing Navier-Stokes equations and boundary conditions to the so-called thin-film

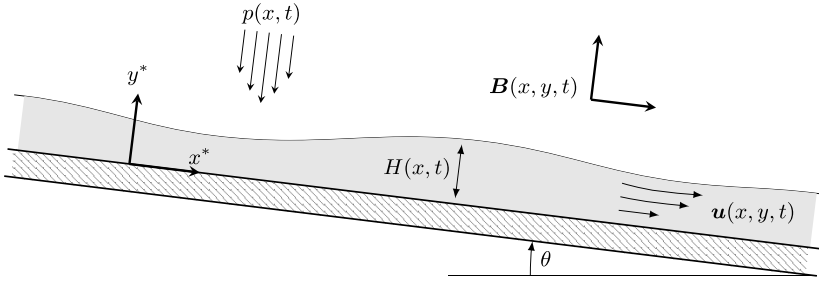


FIG. 1. Schematic of two-dimensional thin-film flow on an inclined plane subject to an externally applied magnetic field  $\mathbf{B}$  and pressure  $p$ .

equation

$$\frac{\partial H}{\partial t} + \frac{\partial}{\partial x} \left[ q(H) \left( 1 - A \frac{\partial p}{\partial x} - \beta \frac{\partial H}{\partial x} + \frac{\partial^3 H}{\partial x^3} \right) \right] = 0 \quad (1)$$

governing the evolution of the free-surface height  $H(x, t)$ . Here  $p(x, t)$  is the dimensionless external applied pressure, with typical amplitude  $A$ , while  $\beta$  is defined by  $\beta = \epsilon \cot \theta$ , where  $\epsilon$  is the small aspect ratio of the thin film and  $\theta$  is the substrate inclination angle. Since  $\theta$  is typically  $O(1)$  in a divertor,  $\beta$  is usually small, which implies that transverse gravitational effects are negligible and surface tension is the main mechanism opposing the free-surface deflections. The function  $q(H)$ , denoting the purely local dependence of the fluid flux on the film height, depends on the precise combination of physical effects included in the model. Versions of (1) were derived in, for example, [1–3].

In a purely hydrodynamical flow,  $q(H) = H^3/3$ . We will present results for the case of Hartmann flow [17] of a magnetic liquid subject to a two-dimensional locally constant magnetic field with components only in the  $(x, y)$  plane. In this case, as shown in the Appendix,

$$q(H) = H \left[ 1 - \frac{\tanh(\text{Ha } H)}{\text{Ha } H} \right], \quad (2)$$

where  $\text{Ha}$  is the Hartmann number, which we will take to be  $\text{Ha} = 10$  in all of our calculations. However, while the numerical results presented here are for this specific magnetohydrodynamic flow, they are qualitatively the same as for the more common hydrodynamic flow: The phenomena described are general, in that they are robust to a wide range of functions  $q$ .

In the absence of the applied pressure, i.e., when  $p = 0$ , the governing equation (1) admits an exact solution where  $H = \text{const} = 1$  without loss of generality. We therefore write

$$H(x, t) = 1 + h(x, t), \quad (3)$$

and the deflection  $h$  of the free surface due to the applied pressure satisfies the equation

$$\frac{\partial h}{\partial t} + \frac{\partial}{\partial x} \left[ Q(h) \left( 1 - A \frac{\partial p}{\partial x} - \beta \frac{\partial h}{\partial x} + \frac{\partial^3 h}{\partial x^3} \right) \right] = 0, \quad (4a)$$

where  $Q(h) = q(H) = q(1 + h)$ . We will consider applied pressure profiles  $p(x, t)$  that are strongly localized in  $x$  and assume that the influence on the free surface is likewise localized so that

$$h \rightarrow 0 \quad \text{as } x \rightarrow \pm\infty. \quad (4b)$$

Finally, we focus on the case of a pressure source that oscillates to and fro in the  $x$  direction. In a tokamak, the plasma exhausted from the core region towards the divertor may be controlled to

sweep the so-called strike point, where the plasma jet impacts the divertor, up and down and thus spread the heat load over a larger area. We are interested in the impact of this oscillating source of momentum on the deflection of the free surface. The general form for such an oscillating pressure will be

$$p(x, t) = \mathcal{P}(x - \ell\mathcal{S}(ft)), \quad (5)$$

where  $\mathcal{P}$  is the stationary pressure profile,  $\ell$  is the sweeping amplitude,  $\mathcal{S}$  is the  $2\pi$ -periodic time profile, and  $f$  is the frequency. For the sake of simplicity, and unless otherwise stated, we will use for  $\mathcal{P}$  a Gaussian centered at zero,

$$\mathcal{P}(x) = e^{-x^2}, \quad (6)$$

and a sinusoidal sweeping profile

$$\mathcal{S}(t) = \sin t. \quad (7)$$

Later on we will demonstrate that the results are robust to changes in the pressure and time-sweeping profiles.

To summarize, in this paper we will investigate how the deflection  $h$  of the free surface of a thin film flowing along a solid substrate, governed by (4), depends on the movement of the pressure source. We note that the problem contains two timescales: the intrinsic relaxation timescale of the free surface and the timescale associated with the imposed pressure oscillations. The dimensionless parameter  $f$  is the ratio of these two timescales and it is therefore natural to split the analysis into three cases:  $f \ll 1$ ,  $f \sim 1$ , and  $f \gg 1$ . We will consider these cases separately. The cases of low and high frequency,  $f \ll 1$  and  $f \gg 1$ , respectively, admit a separation of timescales which allows analytical progress to be made in Secs. III and IV, respectively. The intermediate case  $f \sim 1$  admits no such simplifications, and a full numerical simulation will be carried out and the results described in Sec. V.

### III. SLOW SWEEPING

#### A. Quasisteady approximation

In this section we consider the case of low-frequency oscillations, that is, where  $f \ll 1$ . In this regime, the time it takes for the applied pressure to move a nominal distance is much longer than the time it takes for the free surface to respond to the pressure. Thus the problem becomes quasisteady: To leading order in  $f$ , the free-surface deflection  $h$  attains a steady state which simply translates with the location of the pressure source.

To justify this result formally, we transform to local variables that travel with the moving source by defining

$$\xi = x - \ell\mathcal{S}(ft), \quad \tau = ft \quad (8)$$

so that (4a) becomes

$$f \left( \frac{\partial h}{\partial \tau} - \ell \dot{\mathcal{S}}(\tau) \frac{\partial h}{\partial \xi} \right) + \frac{\partial}{\partial \xi} \left[ Q(h) \left( 1 - A\mathcal{P}'(\xi) - \beta \frac{\partial h}{\partial \xi} + \frac{\partial^3 h}{\partial \xi^3} \right) \right] = 0. \quad (9)$$

Here and henceforth, the prime in  $\mathcal{P}'(\xi)$  is used to denote ordinary differentiation. To leading order in  $f$ , the first term in (9) is negligible and we are left with the ordinary differential equation

$$\frac{d}{d\xi} \left[ Q(h) \left( 1 - A \frac{d\mathcal{P}}{d\xi} - \beta \frac{dh}{d\xi} + \frac{d^3 h}{d\xi^3} \right) \right] = 0 \quad (10)$$

for  $h(\xi)$ . To compute solutions of (10), we implement a full time-dependent solver designed for lubrication-type equations [18] and run the simulation until the solution reaches steady state. An ordinary differential equation solver that directly solves (10) was also implemented for the sake of validation, particularly for cases where  $A$  is large.

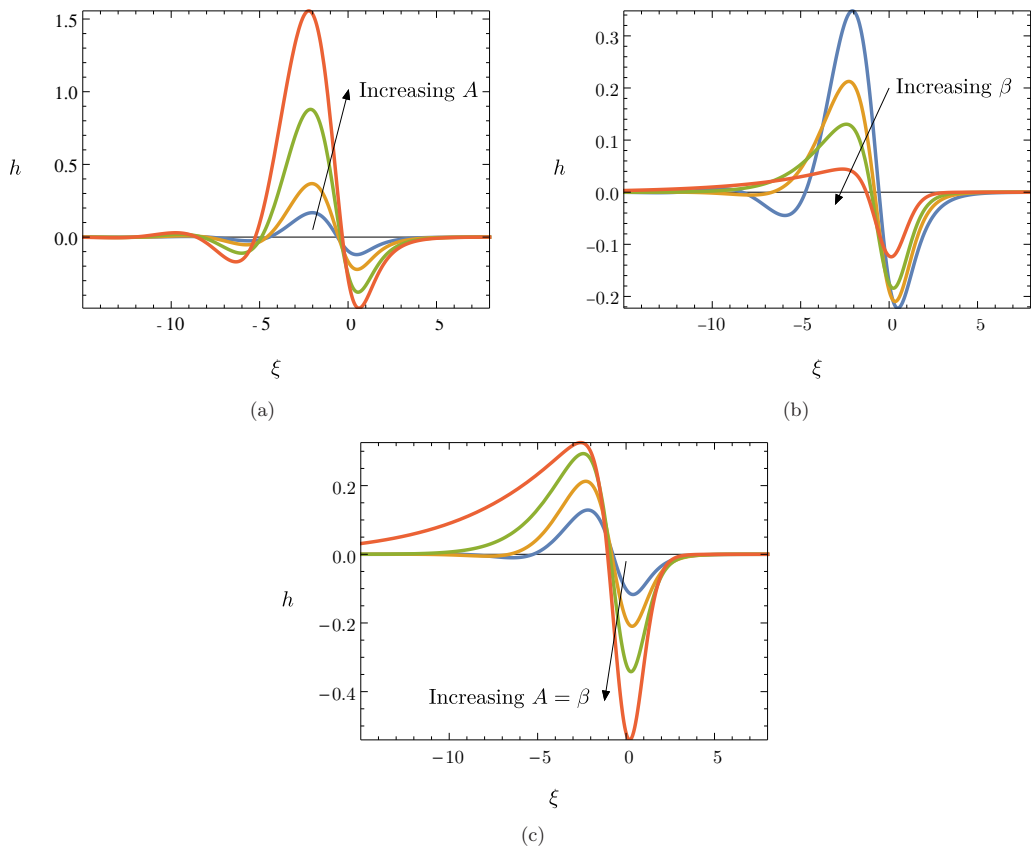


FIG. 2. Steady free-surface deflections  $h(\xi)$  found by numerical solution of (10): (a)  $A \in \{0.5, 1, 2, 3\}$  and  $\beta = 0$ , (b)  $A = 1$  and  $\beta \in \{0.1, 1, 2, 5\}$ , and (c)  $A = \beta \in \{0.5, 1, 2, 5\}$ .

## B. Results

From the numerical simulations shown in Fig. 2, we observe that all solutions are characterized by a peak in the free surface upstream of the strike point  $\xi = 0$  and a trough at or slightly downstream of the strike point. The magnitude of the free-surface displacement increases approximately proportionally to the amplitude  $A$  of the imposed pressure source but decreases with increasing transverse gravitational component  $\beta$ . In Fig. 2(c) we show how these effects compete when both  $A$  and  $\beta$  are increased simultaneously. We see that the deflections become larger, suggesting that, in this setting, the applied pressure is more dominant than transverse gravity. However, we note that, unlike when  $A$  is increased in isolation, the upstream peak is significantly damped and more spread out, so transverse gravity increases the far-field influence of the localized pressure peak. Since both  $A$  and  $\beta$  scale with  $(\sin \theta)^{-2/3}$  as  $\theta \rightarrow 0$  (see the Appendix), Fig. 2(c) could model the effects of decreasing the inclination angle  $\theta$  while keeping everything else constant.

We note that the solutions in Fig. 2 with relatively small values of  $\beta$  exhibit upstream oscillations leading into the strike region, while those with larger values of  $\beta$  do not. To investigate the far-field behavior of the solution, we seek decaying exponential solutions of the form  $h(\xi) \sim e^{\lambda \xi}$  as  $\xi \rightarrow \pm\infty$ . Provided the pressure is a Gaussian (or similar) which vanishes faster than any exponential, it follows from (10) that  $\lambda$  satisfies

$$\lambda^3 - \beta\lambda = -\frac{Q'(0)}{Q(0)} = -L, \quad (11)$$

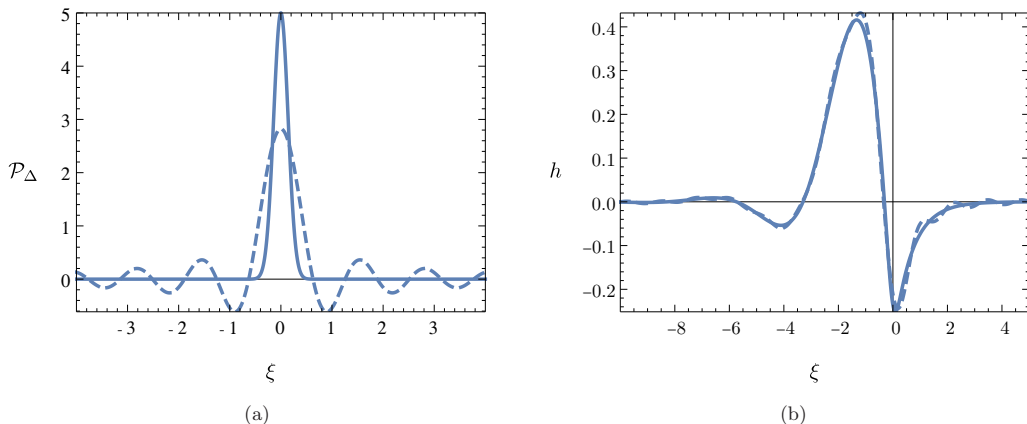


FIG. 3. (a) Nascent  $\delta$  functions  $\mathcal{P}_\Delta$  given by (13) (solid curve) and (14) (dashed curve) where  $\Delta = 0.2$ . (b) Steady-state free-surface profiles, namely, solutions to (10), where  $A = 1$ ,  $\beta = 0$ , and the applied pressures match those from (a).

say. We assume that the flux is a monotonic increasing function of the film height and  $L$  is therefore a positive constant [given by  $L = \text{Ha}(1 + \text{sech}^2 \text{Ha})/(\text{Ha} + \tanh \text{Ha}) \approx 10/11$  for the Hartmann flow flux function (2) with  $\text{Ha} = 10$ ]. Equation (11) always has precisely one real negative root and two other roots with a positive real part. We conclude that the downstream behavior (as  $\xi \rightarrow +\infty$ ) is unconditionally monotonic, while the upstream behavior is either monotonic or oscillatory, depending on whether the two non-negative roots of (11) are real or complex. Elementary manipulation of (11) then reveals that upstream oscillations occur if and only if

$$\frac{\beta^3}{L^2} < \frac{27}{4}. \quad (12)$$

For the Hartmann flow model used in our computations, (12) reduces to  $\beta \lesssim 1.77$ , and indeed we see in Fig. 2(b) that the upstream oscillations are suppressed in the solutions where  $\beta \geq 2$ . As pointed out in Sec. II,  $\beta$  is usually small in practice. Henceforth we will therefore take  $\beta = 0$  in our calculations, in which case (12) is satisfied identically, and we will always expect to observe upstream free-surface oscillations.

### C. Varying the applied pressure

Next we demonstrate that the free-surface profile is robust to the form of the applied pressure  $\mathcal{P}$ . To see this, we consider two families of nascent  $\delta$  functions, a Gaussian family given by

$$\mathcal{P}_\Delta(x) = \frac{1}{\Delta} e^{-(x/\Delta)^2} \quad (13)$$

and a sinc family given by

$$\mathcal{P}_\Delta(x) = \frac{1}{\Delta\sqrt{\pi}} \text{sinc}\left(\frac{x}{\Delta}\right) = \frac{1}{x\sqrt{\pi}} \sin\left(\frac{x}{\Delta}\right). \quad (14)$$

For all positive values of  $\Delta$ , both (13) and (14) satisfy

$$\int_{-\infty}^{\infty} \mathcal{P}_\Delta(x) dx = \sqrt{\pi} \quad (15)$$

and, in the limit  $\Delta \rightarrow 0$ , they each approach a Dirac delta function.

The profiles (13) and (14) are qualitatively different, in that (13) is positive for all  $x$ , while (14) and its derivatives change sign infinitely many times, as shown in Fig. 3(a). Despite this, the different

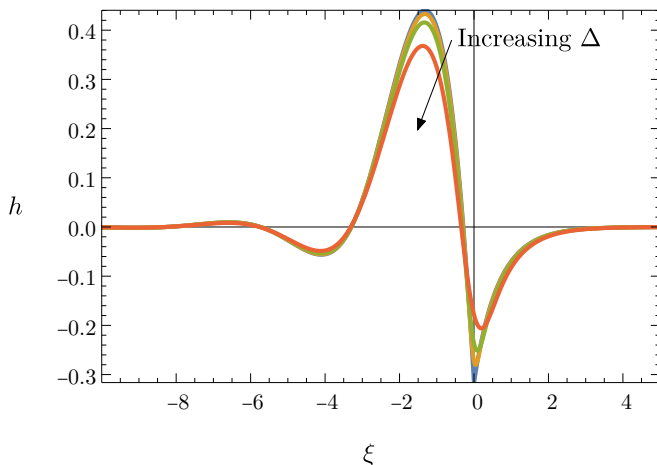


FIG. 4. Steady-state free-surface profiles, namely, solutions to (10), where  $A = 1$ ,  $\beta = 0$ , and the applied pressure is given by (13) with  $\Delta \in \{0.001, 0.1, 0.2, 0.4\}$ .

pressure profiles produce very similar free-surface deflections, as shown in Fig. 3(b). These results highlight the fact that, provided the pressure source is localized, the free-surface profile is shaped largely by capillarity and not by the particular form of  $\mathcal{P}$  away from the origin. For the sake of numerical simplicity, we will henceforth continue to use a Gaussian in simulations.

Furthermore, we note the similarity between free-surface profiles for a wide range of the characteristic width parameter  $\Delta$ , as illustrated in Fig. 4. For larger  $\Delta$ , the pressure profile is more spread out and the resulting deflection profile exhibits somewhat damped peaks and troughs. As  $\Delta$  decreases, we see a sharper transition local to the origin as Eq. (10) becomes singular there. In the limit  $\Delta \rightarrow 0$ , we see that  $\mathcal{P}$  approaches a  $\delta$  function which forces a jump discontinuity in the first derivative of  $h$ . The continuity of  $h(\xi)$ , as well as the jump discontinuity in  $h'(\xi)$  of magnitude  $A\sqrt{\pi} \approx 1.77$  when  $A = 1$ , can be observed in Fig. 4.

#### D. Large-amplitude applied pressure

The solutions plotted in Fig. 2 demonstrate that, unsurprisingly, the magnitude of the free-surface deflection  $h$  increases as the amplitude  $A$  of the imposed pressure increases and as the gravitational parameter  $\beta$  decreases. However, we will now argue that, however large the applied pressure, it is impossible for the deflection ever to become so large that the film thickness  $H$  reaches zero, which would correspond to drying out of the liquid film. To see this, we integrate (10), applying vanishing boundary conditions to both the pressure and the deflection to give

$$1 - \beta \frac{dh}{d\xi} + \frac{d^3h}{d\xi^3} = \frac{Q(0)}{Q(h)} + A \frac{d\mathcal{P}}{d\xi}. \quad (16)$$

If the pressure gradient is large enough for the film thickness  $H = h + 1$  to approach zero, then the flux function  $Q(h) = q(H)$  likewise approaches zero. For the Hartmann flow flux function (2) used in our simulations, we have  $q(H) = O(H^3)$  when  $H \ll 1/\text{Ha}$ . A dominant balance in (16) then suggests the scaling law

$$\min H \propto \left( -A \frac{d\mathcal{P}}{d\xi} \right)^{-1/3} \quad \text{when} \quad -A \frac{d\mathcal{P}}{d\xi} \gg 1, \quad H \ll 1/\text{Ha}. \quad (17)$$

There is also an intermediate regime where  $1/\text{Ha} \ll H \ll 1$ . In this case the flux function, to leading order in  $(\text{Ha} H)^{-1}$ , satisfies  $q(H) = O(H)$ , and then a dominant balance in (16) suggests

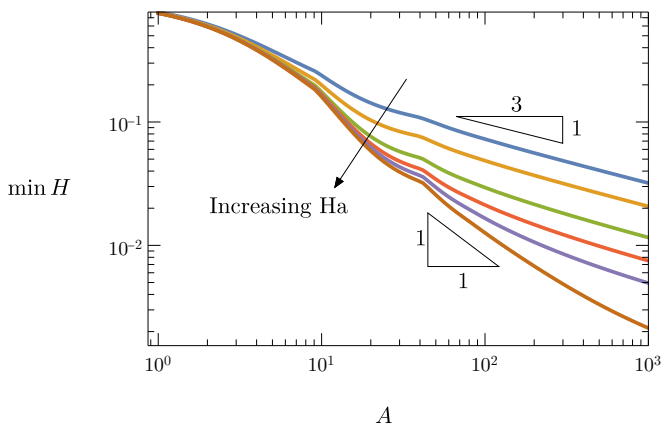


FIG. 5. Minimal film thickness as a function of the applied pressure amplitude  $A$ , where  $Ha \in \{10, 20, 50, 100, 200, 1000\}$  and  $\beta = 0$ .

that

$$\min H \propto \left(-A \frac{d\mathcal{P}}{d\xi}\right)^{-1} \quad \text{when } -A \frac{d\mathcal{P}}{d\xi} \gg 1, \quad 1/Ha \ll H \ll 1. \quad (18)$$

Both of the scalings (17) and (18) can be observed in our numerical simulations. As illustrated in Fig. 5, the minimum film thickness scales with  $A^{-1/3}$  as the amplitude  $A$  of the applied pressure tends to infinity, while for large enough  $Ha$  there is an intermediate region where the minimum film thickness scales with  $A^{-1}$ .

In general, even if other physics is included, viscous hydrodynamic effects will usually dominate when the film thickness is small. We can therefore expect the limiting behavior  $q(H) = O(H^3)$ , and consequently the dependence (17) of the minimum thickness on the applied pressure gradient, to be quite general, at least for flow with no slip on a rigid substrate. We conclude that, although the minimum film thickness tends to zero as  $A \rightarrow \infty$ , it can never reach zero as long as the applied pressure remains finite.

#### IV. FAST SWEEPING

If  $f \gg 1$ , then the characteristic timescale on which the applied pressure sweeps is significantly faster than the time it takes for the fluid to deform under the applied pressure. In this case we can expect the sweeping to have the effect of spreading the momentum load just as it does the heat load. To analyze this limit, we pose a multiple scales ansatz, where the slow-time variable  $t$  and the fast variable  $\tau = ft$  are considered independent. Moreover, we assume that  $h(x, t, \tau)$  is  $2\pi$  periodic with respect to  $\tau$  and that the applied pressure has no slow-time dependence, that is,

$$p(x, \tau) = \mathcal{P}(x - \ell\mathcal{S}(\tau)). \quad (19)$$

We then pose the asymptotic expansion

$$h \sim h_0 + \frac{1}{f}h_1 + \dots \quad (20)$$

and find that the leading-order term is a function only of the slow timescale:  $h_0 = h_0(x, t)$ .

At  $O(1/f)$ , the solvability condition for  $h_1$  provides an evolution equation for the leading-order film thickness, namely,

$$\frac{\partial h_0}{\partial t} + \frac{\partial}{\partial x} \left[ Q(h_0) \left( 1 - A \frac{d\bar{p}}{dx} - \beta \frac{\partial h_0}{\partial x} + \frac{\partial^3 h_0}{\partial x^3} \right) \right] = 0, \quad (21a)$$

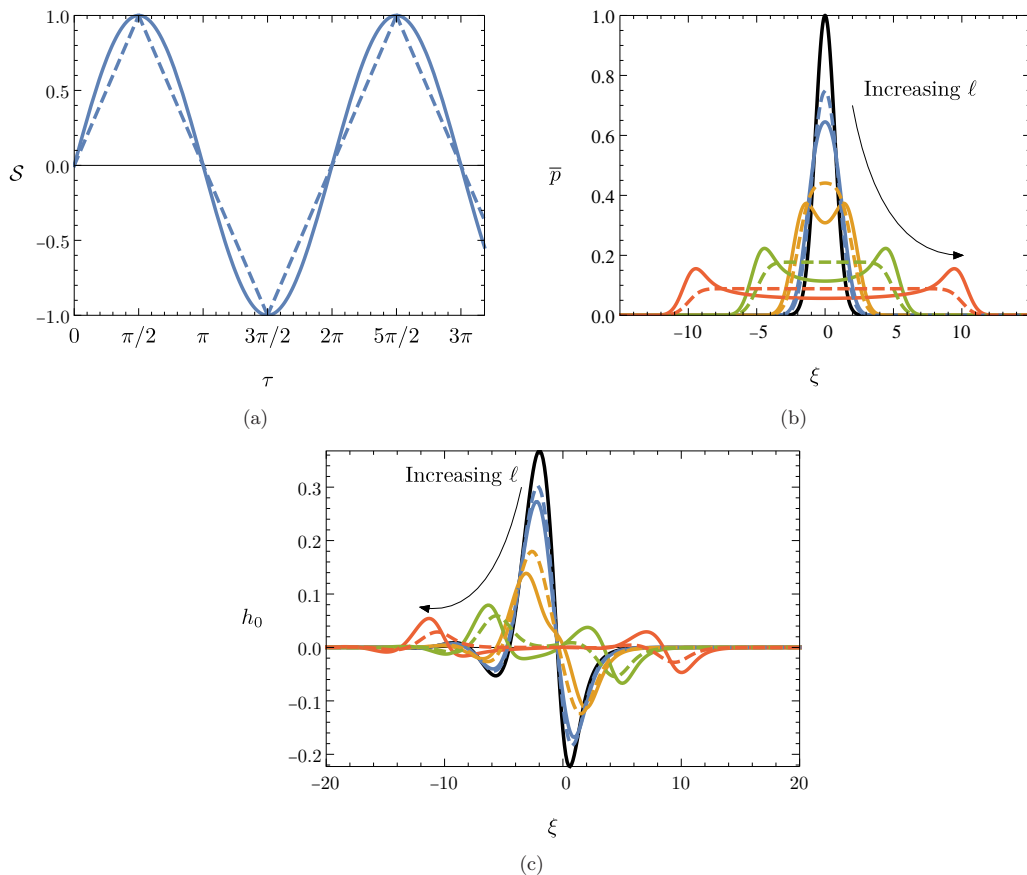


FIG. 6. (a) Sweeping profiles  $S(\tau)$ :  $S(\tau) = \sin \tau$  is the solid curve and the dashed curve shows a triangle wave that linearly interpolates the peaks and troughs of the sine curve. (b) Time-averaged applied pressure profiles calculated from (21b) with both fast-time functions from graph (a) and  $\ell \in \{0, 1, 2, 5, 10\}$ . (c) Steady multiple-scale solutions of (21) for the averaged profiles in graph (b) where  $A = 1$  and  $\beta = 0$ .

where

$$\bar{p}(x) = \frac{1}{2\pi} \int_0^{2\pi} p(x, \tau) d\tau. \quad (21b)$$

Equation (21a) is identical to (4a) except that the applied pressure is replaced by a time-independent *effective applied pressure* which has been averaged over the fast timescale. This analysis therefore confirms the earlier stated intuition that the effect of sufficiently fast sweeping is to spread the momentum load.

The solid curves in Fig. 6(b) show the effective pressure profile  $\bar{p}(x)$  for a Gaussian underlying pressure source (6), a sinusoidal sweeping profile (7), and various values of the sweeping amplitude  $\ell$ . We observe that the larger the amplitude  $\ell$  of the oscillations, the smaller the magnitudes of the maximal and minimal pressure and the wider the region over which the profile is spread, as expected. For sufficiently large  $\ell$ , the effective pressure profile produced with a sinusoidal sweeping profile  $S(\tau)$  exhibits a peak at either end, where  $S(\tau)$  is stationary, so the pressure maximum lingers there. For comparison, we show using dashed curves the corresponding effective pressures when the sweeping profile  $S(\tau)$  is a triangle wave, and these end peaks do not appear. Nevertheless, for small

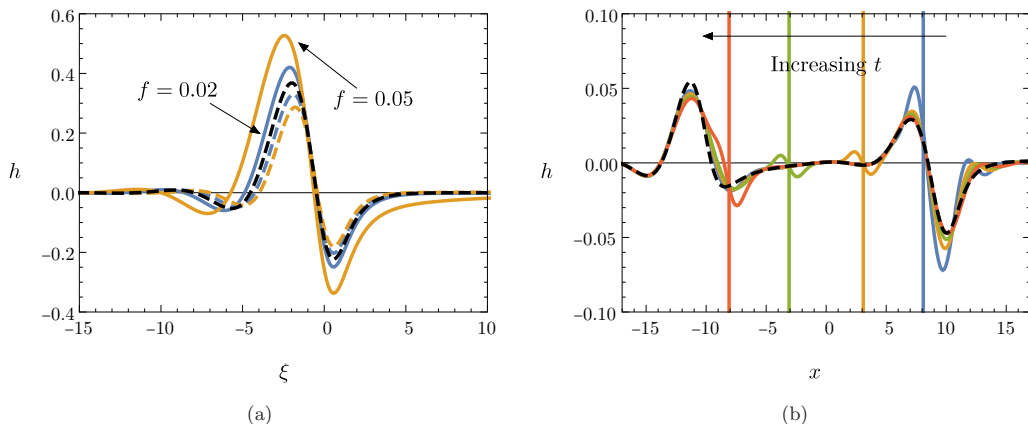


FIG. 7. (a) Time-dependent numerical solutions of the problem (4) with  $\ell = 10$ , evaluated at  $t = \pi$  (dashed curve) and  $t = 2\pi$  (solid curve), with  $f = 0.02$  (blue) and  $f = 0.05$  (orange); the black dashed curve shows the quasisteady solution to (10) valid in the limit  $f \rightarrow 0$ . (b) Time-dependent numerical solution of the problem (4) with  $\ell = 10$  and  $f = 10 \gg 1$ , evaluated at  $t/\pi = 14 + (1/2 + i/5)/f$ , for  $i = 1, 2, 3, 4$ ; the vertical lines show the center of the applied pressure profile at each value of  $t$ . The black dashed curve shows the steady solution of (21), valid in the limit  $f \rightarrow \infty$ . Movies of the time-dependent simulations shown in this figure are included in the Supplemental Material [19].

values of  $\ell$  it is the sinusoidal  $\mathcal{S}(\tau)$  that produces the smaller magnitude effective pressure and pressure gradient.

Since the effective pressure  $\bar{p}(x)$  is time independent, the solution  $h_0$  of (21a) ultimately converges to a steady state, as will be demonstrated below in Sec. V A by direct numerical simulation. We compute the steady-state solution  $h_0(x)$  of (21) using the same procedure as that used for the regime where  $f \ll 1$  in Sec. III, and results are illustrated in Fig. 6(c). We find that the steady profiles, like the effective pressures, exhibit smaller deflections for larger values of the sweeping amplitude  $\ell$ . Similarly to the pressure profiles, for small values of  $\ell$  sinusoidal oscillations cause smaller free-surface deflections than the triangle-wave sweeping profile  $\mathcal{S}(\tau)$ , while for larger values of  $\ell$  the situation is reversed.

In summary, the analysis of this section confirms that lateral oscillations of the pressure source at sufficiently high frequency can indeed be used to spread the momentum load and significantly reduce the deflection of the thin film.

## V. INTERMEDIATE SWEEPING

### A. Numerical investigation

In Secs. III and IV we have shown that the equilibrium free-surface deflection problem becomes effectively steady in the limits of both low-frequency and high-frequency sweeping. In the former case, the governing equation (10) is quasisteady and the free-surface deflection depends only parametrically on the location of the pressure source; in the latter case, the governing equation (21a) is driven by a steady time-averaged effective pressure  $\bar{p}(x)$  and the deflection ultimately reaches a steady state, possibly after some transient.

The accuracy of these asymptotic limits is illustrated in Fig. 7. In Fig. 7(a) we show time-dependent numerical solutions computed with small but nonzero values of  $f$ . As the value of  $f$  increases, the difference between the solutions evaluated at two different values of  $t$  tends to zero, indicating that the solution is becoming quasisteady, and both converge to the solution of (10), which is valid in the limit  $f \rightarrow 0$ . In Fig. 7(b) we show time-dependent numerical solutions computed with a large but finite value of  $f$ . The simulation is first run up to  $t = 14\pi$ , allowing initial transients

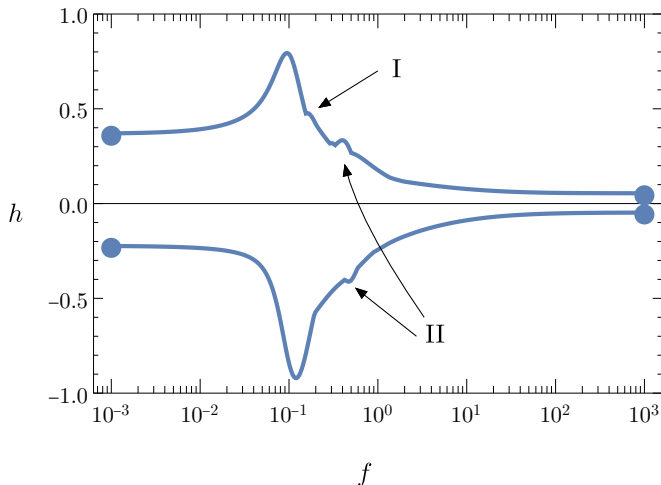


FIG. 8. Extremal free-surface deflections  $\liminf h$  and  $\limsup h$  as functions of the sweeping frequency  $f$ , where  $\ell = 10$ ,  $A = 1$ , and  $\beta = 0$ . The extrema of the leading-order solutions as  $f \rightarrow 0$  and as  $f \rightarrow \infty$  are marked by disks. Labels I and II mark anomalous local behaviors discussed in Sec. V D.

to decay, and then we plot time intervals corresponding to half-oscillations. We observe a small localized ripple that follows the locus of the moving pressure source (indicated by the vertical lines), but otherwise the solution remains close to the steady solution of the multiple-scale model (21), valid in the limit  $f \rightarrow \infty$ .

In this section we study the intermediate regime of moderate frequency by direct numerical simulation of (4) to compute the deflection  $h(x, t)$ . When  $f = O(1)$ , the applied pressure contains an order-unity time dependence and there exists no steady-state solution for  $h(x, t)$ . To compare results from this regime to those from Secs. III and IV, we must therefore consider some relevant functionals of the solution  $h$ . In the context of a divertor, the main focus is to maintain small deflections and thus it is natural to consider the supremal and infimal deflections  $\sup_{x,t} h(x, t)$  and  $\inf_{x,t} h(x, t)$ . To remove the dependence of these functionals on the arbitrary initial conditions, we will consider the limit extrema  $\lim_{T \rightarrow \infty} \sup_{|x| < X, t > T} h(x, t)$  and  $\lim_{T \rightarrow \infty} \inf_{|x| < X, t > T} h(x, t)$  for some large  $X$  and  $T$ . We compute these by running the simulations for large times, taking  $X \gg \ell$ , and excluding an initial period of time  $T$  such that deflections caused by initial conditions have propagated beyond the  $|x| < X$  window.

In Fig. 8 we plot the extreme values of the displacement, computed as described above, versus the dimensionless frequency  $f$  with the other parameter values  $\ell = 10$ ,  $A = 1$ , and  $\beta = 0$ . As  $f$  becomes very small, both  $\liminf h$  and  $\limsup h$  become independent of  $f$  and approach constant values in agreement with results of the  $f \rightarrow 0$  analysis from Sec. III, which are indicated by disks in Fig. 8. For very large values of  $f$ , the extremal values of  $h$  likewise approach constant values, which are somewhat smaller due to the spreading effect of the pressure sweeping, and also consistent with results of the multiple-scale analysis from Sec. IV. However, as  $f$  increases from small to large values, the extremal deflections do not vary monotonically, but increase to a significant peak at a critical intermediate value of the frequency  $f$  before decreasing again. This apparent resonance occurs when the applied pressure sweeps at a similar speed to the propagation speed of free-surface deformations, so the pressure peak spends a long time at the trough in the free surface. We will explore this effect in Sec. V B by analyzing traveling-wave solutions of (4) for the simpler case where the pressure source moves at constant speed.

In Fig. 9 we show the effects on the response diagram of varying the pressure source amplitude  $A$  and the sweeping amplitude  $\ell$ . Unsurprisingly, the free-surface response increases roughly proportionally to the forcing amplitude  $A$ . As  $\ell$  increases, the principal peaks in the response occur

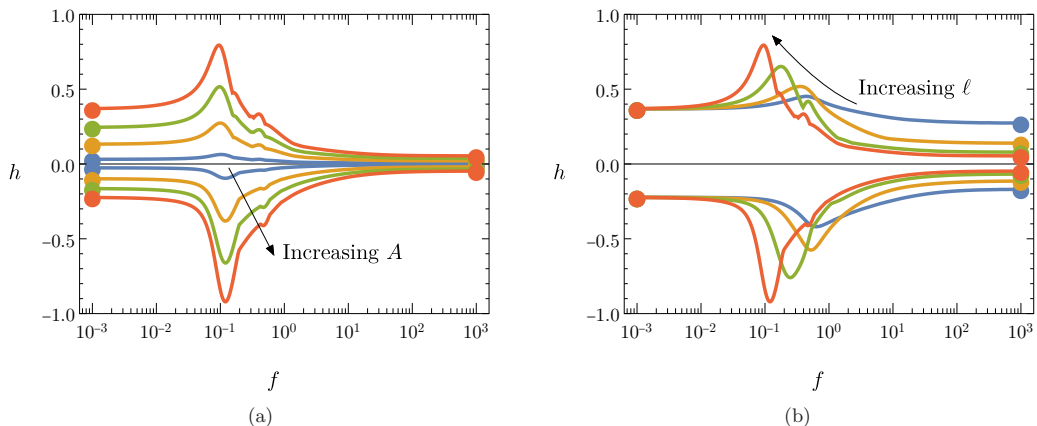


FIG. 9. Extremal free-surface deflections  $\liminf h$  and  $\limsup h$  as functions of the sweeping frequency  $f$ , where  $\alpha = 1$ ,  $\beta = 0$ , and (a)  $\ell = 10$  and  $A \in \{0.1, 0.4, 0.7, 1\}$  and (b)  $A = 1$  and  $\ell \in \{1, 2, 5, 10\}$ .

at smaller values of  $f$  such that  $\ell f \sim 1$ , corresponding to keeping the maximum sweeping velocity constant. The magnitude of the response also increases with increasing  $\ell$ , since the pressure source then spends longer moving close to the intrinsic propagation speed of free-surface disturbances. This effect will be explored further in Sec. VC by studying the local behavior when the sweeping speed is not constant but stationary at the intrinsic propagation speed. Finally, in Sec. VD we explore the appearance of smaller local peaks in the free-surface response, for example, those labeled I and II in Fig. 8.

### B. Traveling waves

To investigate the origin of the peak in the response diagram in Fig. 8, we first consider traveling-wave solutions with constant wave speed  $V$ . For applied pressure and free-surface deflection of the forms  $p(x, t) = \mathcal{P}(\xi)$  and  $h(x, t) = h(\xi)$ , with  $\xi = x - Vt$ , the governing equation (4) reduces to the ordinary differential equation

$$\frac{d^3 h}{d\xi^3} = A \frac{d\mathcal{P}}{d\xi} - 1 + \frac{Q(0) + Vh}{Q(h)} \quad (22)$$

when the transverse gravitational parameter  $\beta$  is assumed to be negligible. In principle, Eq. (22) can be solved numerically, subject to  $h \rightarrow 0$  as  $\xi \rightarrow \pm\infty$ . Versions of Eq. (22) have been studied previously with various forms of the flux function  $Q$  and the forcing term  $\mathcal{P}$ , for example, in [14–16], all of which report that the solution of the steady nonlinear problem may exhibit nonexistence and nonuniqueness. We are especially interested in how the amplitude of the response depends on the traveling-wave speed  $V$ , and we will see that useful insight may be gained by considering the linearized problem for small  $h$ .

Let us therefore consider the case where the amplitude  $A$  of the applied pressure is small. The free-surface deflection  $h$  is then likewise expected to be of order  $A$ , and to leading order in  $A$  Eq. (22) reduces to the linearized equation

$$\frac{d^3 h}{d\xi^3} + Lh = A \frac{d\mathcal{P}}{d\xi}, \quad (23)$$

where

$$L = \frac{Q'(0) - V}{Q(0)}. \quad (24)$$

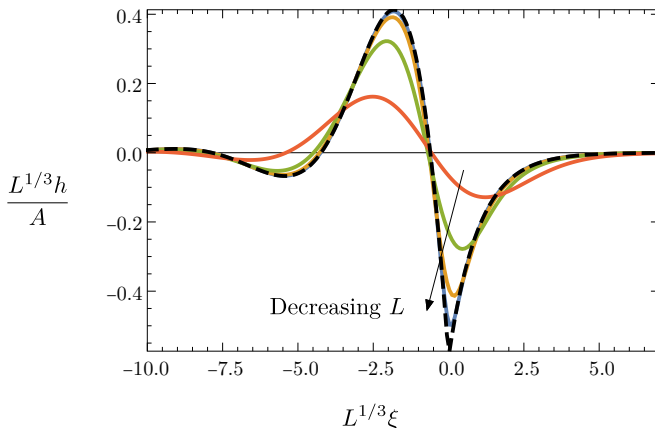


FIG. 10. Solutions of the linear traveling-wave problem (23) with Gaussian applied pressure  $\mathcal{P}(\xi) = e^{-\xi^2}$  given in (25), where  $L \in \{0.01, 0.1, 1, 10\}$ . The dashed curve shows the limit as  $L \rightarrow 0$  given by (26).

For a stationary frame, with  $V = 0$ , the definition (24) of  $L$  is equivalent to the previous definition in (11) from Sec. III B. When  $V$  is nonzero  $L$  need not be positive but, provided the pressure profile  $\mathcal{P}(\xi)$  is even, we can nevertheless restrict our attention to non-negative values of  $L$  by exploiting the invariance of Eq. (23) under the transformation  $(\xi, L) \mapsto (-\xi, -L)$ . Thus a solution of (23) with  $L < 0$  can be obtained by just flipping the sign of  $\xi$  in the corresponding solution where the sign of  $L$  is flipped.

The solution of (23) with  $L > 0$ , subject to vanishing far-field conditions, may be written in the form

$$h(\xi) = -\frac{A}{3L^{2/3}} \int_0^\infty \left\{ e^{-s\mathcal{P}\left(\xi - \frac{s}{L^{1/3}}\right)} + 2e^{-s/2} \cos\left(\frac{\sqrt{3}s}{2} + \frac{\pi}{3}\right) \mathcal{P}\left(\xi + \frac{s}{L^{1/3}}\right) \right\} ds. \quad (25)$$

In Fig. 10 we plot typical solutions for  $h(\xi)$ , where we have used a Gaussian pressure profile. We observe that the free-surface displacement scales with  $A/L^{1/3}$  and approaches a function of  $L^{1/3}\xi$  as  $L \rightarrow 0$ , and the variables in Fig. 10 are scaled accordingly. The limiting behavior as  $L \rightarrow 0$  resembles that seen previously in Fig. 4: Decreasing the value of  $L$  increases the natural relaxation length scale of the system, which effectively makes the applied pressure source more localized. By approximating  $\mathcal{P}$  by a  $\delta$  function, the leading-order solution in this limit is thus found to be given by

$$h \sim -\frac{A\sqrt{\pi}}{3L^{1/3}} \begin{cases} 2e^{L^{1/3}\xi/2} \cos\left(\frac{\sqrt{3}L^{1/3}\xi}{2} - \frac{\pi}{3}\right), & \xi < 0 \\ e^{-L^{1/3}\xi}, & \xi > 0, \end{cases} \quad (26)$$

which is plotted as a black dashed curve in Fig. 10.

We deduce that, as  $L \rightarrow 0$ , the solution  $h(\xi)$  of the linear equation (23) becomes unbounded, with magnitude of order  $L^{-1/3}$ , while the minimum in the film thickness approaches the strike point  $\xi = 0$ . This is true in particular when the applied pressure profile is Gaussian, but also whenever the pressure is localized such that  $\mathcal{P}(s/L^{1/3})$  approaches a  $\delta$  function as  $L \rightarrow 0$ . The linearization that gave rise to Eq. (23) is only valid if the amplitude of the solution is sufficiently small, i.e., if  $A/L^{1/3}$  is sufficiently small. Traveling-wave solutions with  $O(1)$  amplitude satisfy the nonlinear equation (22). However, in Fig. 11(a) we show that numerical solutions of (22) are well approximated by the linearized solution (25), even for moderate values of  $A$ . Figure 11(b) shows numerical solutions of the nonlinear traveling-wave equation (22) for different values of the wave speed  $V$ . The qualitative behavior is similar to the linearized solutions shown in Fig. 10. There is an apparent symmetry as the

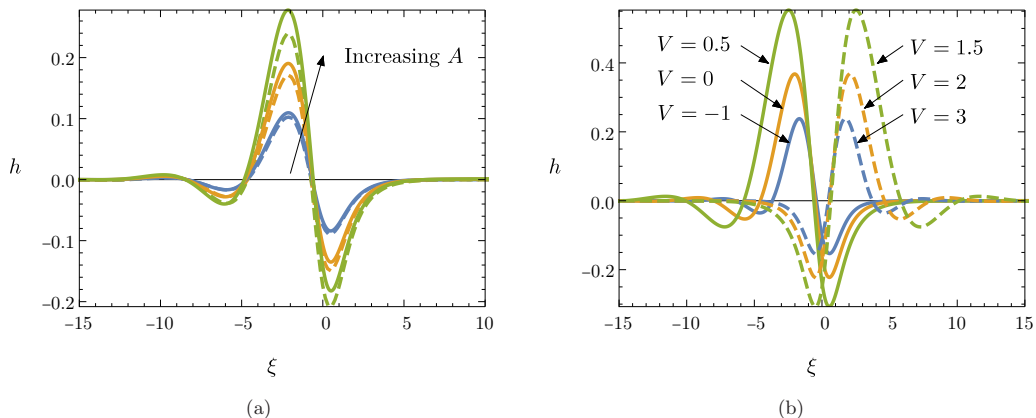


FIG. 11. (a) Solutions of the nonlinear traveling-wave equation (22) (solid curves) compared with solutions of the linearized equation (23) (dashed curves) where  $V = 0.2$  and the applied pressure profile is the Gaussian (6) with amplitude  $A \in \{0.3, 0.5, 0.7\}$ . (b) Solutions of the nonlinear traveling-wave equation (22) with  $A = 1$ , Gaussian pressure profile (6), and values of  $V$  as indicated.

signs of  $\xi$  and  $L \approx 1 - V$  are switched, and the amplitude of the response increases dramatically as  $V$  approaches 1, corresponding to  $L \approx 0$ .

The analysis of this section shows that, for a pressure source moving at constant speed, the maximum negative free-surface deflection is expected to occur when the parameter  $L$  is small, i.e., when the propagation speed  $V$  is close to the characteristic speed  $Q'(0)$  of the underlying hyperbolic version of the partial differential equation (PDE) (4). For the case of sinusoidal sweeping of the pressure source, the propagation speed is obviously not constant, but it is instantaneously stationary at its maximum and minimum values, namely,  $\pm V_{\max}$  where  $V_{\max} = \ell f$ . We therefore hypothesize that the minimum film thickness in this case should occur when  $\ell f = Q'(0) \approx 1$  for the Hartmann flux function (2) with  $Ha \gg 1$ . This hypothesis is confirmed in Fig. 12(a), where we plot the value of  $f$  that minimizes  $h$  versus  $\ell$ . Since the magnitude of the response increases with increasing  $\ell$ , we use gradually decreasing values of the pressure amplitude  $A$  such that the film thickness does

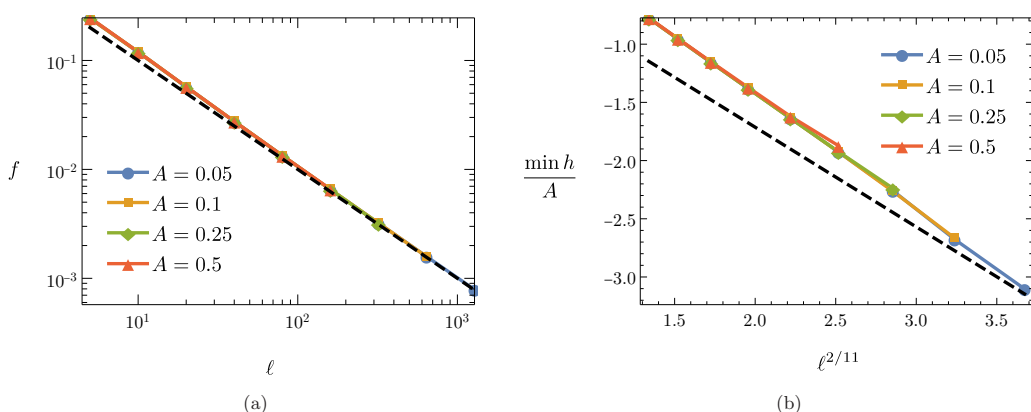


FIG. 12. (a) Sweeping frequency  $f$  that minimizes the film thickness  $h$  in the full nonlinear simulation plotted versus sweeping amplitude  $A$  for a range of values of the pressure amplitude  $A$ . The black dashed curve shows the behavior  $\ell f \sim 1$  predicted for  $\ell \gg 1$ . (b) Minimal deflection  $h$  normalized by  $A$ , computed from the full nonlinear simulation, as a function of  $\ell^{2/11}$ , for various values of the pressure amplitude  $A$ . The black dashed curve shows the asymptotic prediction (35), which corresponds here to  $\min h/A \sim -0.856681\ell^{2/11}$ .

not become too small. It is evident that, as  $\ell$  increases, the behavior converges to the predicted trend  $\ell f \sim 1$ , which is marked as a black dashed curve.

In Fig. 12(b) we show how the minimum film thickness varies with the sweeping amplitude  $\ell$ ; as in Fig. 12(a), steadily decreasing values of  $A$  are used to prevent  $h$  from becoming too small. We note that the results computed with different values of  $A$  appear to collapse when  $h$  is normalized with  $A$ . Moreover, as  $\ell$  increases, the minimum film thickness decreases, in agreement with Fig. 9. Figure 12(b) indicates that  $\min h/A$  scales with  $\ell^{2/11}$  when  $\ell$  is large, for reasons that will be explained in the next section, by exploring in more detail the behavior when the propagation speed is stationary but not constant.

### C. Perturbed traveling-wave problem

We recall that the free-surface displacement  $h$  in a frame that propagates with the moving pressure source is governed by the PDE (9), which may be written in the form

$$f \frac{\partial h}{\partial \tau} + \frac{\partial}{\partial \xi} \left[ -\ell f \dot{S}(\tau) h + Q(h) \left( 1 - A \mathcal{P}'(\xi) + \frac{\partial^3 h}{\partial \xi^3} \right) \right] = 0, \quad (27)$$

when the parameter  $\beta$  is neglected. To investigate the behavior seen in Fig. 9, we wish to consider solutions where the sweeping amplitude  $\ell$  is large but the frequency  $f$  is small such that their product is order one. At first glance, it appears that the first term in (27) is then negligible, and the problem becomes quasisteady, reducing to the traveling-wave equation (22) with the propagation speed  $V$  depending parametrically on  $\tau$ . However, we have argued above in Sec. VB that large-amplitude response is expected when  $V$  is close to the characteristic speed  $Q'(0)$  and indeed the linearized equation (23) has no bounded solutions when  $V = Q'(0)$ . We therefore seek in this section a distinguished limit where  $V(\tau)$  is stationary at the critical value  $Q'(0)$  and the local behavior is fully unsteady.

We simplify matters by again linearizing for small  $|h|$  and  $A$  and restrict our attention to sinusoidal sweeping with  $S(\tau) = \sin \tau$ . The sweeping velocity  $V(\tau) = \ell f \dot{S}(\tau) \approx \ell f (1 - \tau^2/2)$  is stationary at  $\tau = 0$ , and we take  $\ell f = Q'(0)$  so that the stationary velocity is equal to the characteristic value  $Q'(0)$ . Thus, close to  $\tau = 0$ , Eq. (27) may be approximated by

$$\frac{f}{Q(0)} \frac{\partial h}{\partial \tau} + \frac{\ell f}{2Q(0)} \tau^2 \frac{\partial h}{\partial \xi} + \frac{\partial^4 h}{\partial \xi^4} = A \mathcal{P}''(\xi). \quad (28)$$

We normalize (28) with the scalings

$$\tau = \left( \frac{Q(0)}{Q'(0)} \right)^{1/11} \ell^{-3/11} T, \quad \xi = \left( \frac{Q(0)}{Q'(0)} \right)^{3/11} \ell^{2/11} X, \quad h = A \left( \frac{Q(0)}{Q'(0)} \right)^{3/11} \ell^{2/11} Y. \quad (29)$$

When  $\ell \gg 1$ , the scalings (29) correspond to asymptotically small values of  $\tau$ , which justifies *a posteriori* our Maclaurin expansion of the propagation speed  $V(\tau)$ . Moreover, the scale for  $\xi$  is asymptotically large, which implies that the pressure forcing term  $\mathcal{P}(\xi)$  may be approximated by a  $\delta$  function over  $O(1)$  values of  $X$ , as in the small- $L$  limit from Sec. VB. Thus, to lowest order as  $\ell \rightarrow \infty$ , Eq. (28) reduces to the canonical PDE

$$\frac{\partial Y}{\partial T} + \frac{T^2}{2} \frac{\partial Y}{\partial X} + \frac{\partial^4 Y}{\partial X^4} = \sqrt{\pi} \delta''(X). \quad (30)$$

The solution of (30) subject to  $Y(X, T) \rightarrow 0$  as  $X \rightarrow \pm\infty$  and as  $T \rightarrow -\infty$  may be written in the form

$$Y(X, T) = -\frac{2}{\sqrt{\pi}} \int_0^\infty G \left( \frac{X}{s} - \frac{T^2 s^3}{2} + \frac{T s^7}{2} - \frac{s^{11}}{6} \right) ds, \quad (31)$$

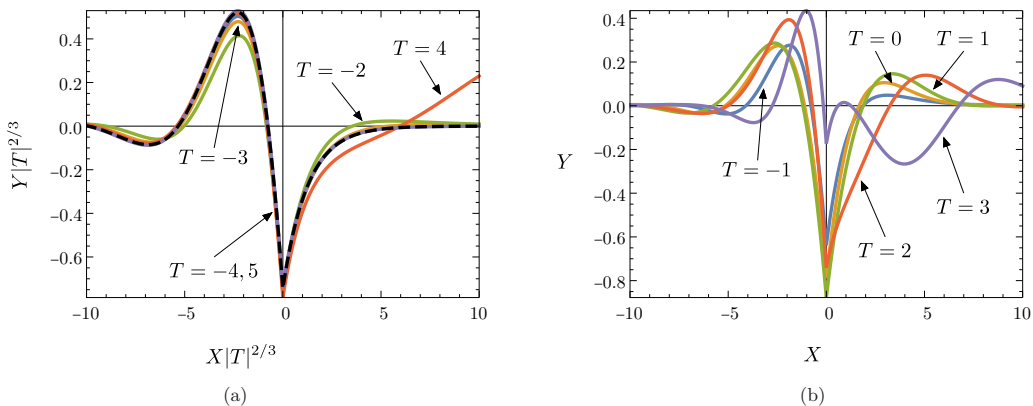


FIG. 13. Solution  $Y(X, T)$  given by Eq. (31) plotted versus  $X$  for (a) larger values of  $|T|$  and (b) smaller values of  $|T|$ . In (a), the variables  $X$  and  $Y$  are scaled with  $|T|^{2/3}$  to reflect the self-similarity, and the limiting solution as  $|T| \rightarrow \infty$ , given by (33), is plotted as a dotted black curve; the solutions for  $T = -4$  and  $T = 5$  are virtually indistinguishable from the limiting solution.

where

$$G(z) := \int_{-\infty}^{\infty} k^2 e^{-k^4 + ikz} dk = \frac{\Gamma(3/4)}{2} {}_0F_2\left(\frac{1}{4}; \frac{1}{2}; \frac{z^4}{256}\right) - \frac{\Gamma(1/4)}{16} z^2 {}_0F_2\left(\frac{3}{4}; \frac{3}{2}; \frac{z^4}{256}\right), \quad (32)$$

with  ${}_0F_2$  denoting a generalized hypergeometric function. The solution (31) is plotted versus  $X$  for various values of  $T$  in Fig. 13. As  $|T| \rightarrow \infty$ , the solution becomes self-similar, with

$$Y(X, T) \sim -\frac{2^{1/3}\sqrt{\pi}}{3|T|^{2/3}} \begin{cases} 2e^{X|T|^{2/3}/2^{4/3}} \cos\left(\frac{\sqrt{3}X|T|^{2/3}}{2^{4/3}} - \frac{\pi}{3}\right), & X < 0 \\ e^{-X|T|^{2/3}/2^{1/3}}, & X > 0, \end{cases} \quad (33)$$

which matches with the traveling-wave solution (26). In Fig. 13(a) we scale  $X$  and  $Y$  with  $|T|^{2/3}$  to demonstrate convergence to the similarity solution (33), which is plotted as a dashed black curve.

It follows from (33) that the behaviors as  $T \rightarrow -\infty$  and as  $T \rightarrow +\infty$  are equivalent but, as shown in Fig. 13(b), the behavior when  $T = O(1)$  does not respect this symmetry. In particular, we observe that the minimum value of  $Y$  occurs at  $X = 0$  when  $T \approx 1$ . This observation is supported by Fig. 14, where we plot the normalized displacement at the origin  $Y(0, T)$  versus  $T$ . The red dashed curves demonstrate convergence to the similarity solution (33), with

$$Y(0, T) \sim -\frac{2^{1/3}\sqrt{\pi}}{3|T|^{2/3}} \quad \text{as } |T| \rightarrow \infty. \quad (34)$$

The minimum value of  $Y(0, T)$  is approximately  $-0.881655$  when  $T \approx 1.19518$ . By undoing the scalings (29), we infer that the minimal free-surface displacement  $h$  should behave like

$$\min h \sim -0.881655 \left(\frac{Q(0)}{Q'(0)}\right)^{3/11} \ell^{2/11}, \quad (35)$$

when  $\ell \gg 1$  and  $\ell f \sim Q'(0)$ . Figure 12(b) shows fairly good convergence of our computed numerical solutions to the predicted behavior (35), which is plotted as a black dashed curve. Because of the very small exponent  $2/11$ , extremely large values of  $\ell$  are needed for the predicted behavior (35) to convincingly emerge.

Since we have only analyzed the linearized version of the problem, these results are only strictly valid while the free-surface displacement remains relatively small; this is why we reduce the value of  $A$  while increasing the value of  $\ell$  in the results shown in Fig. 12. Nevertheless, our analysis

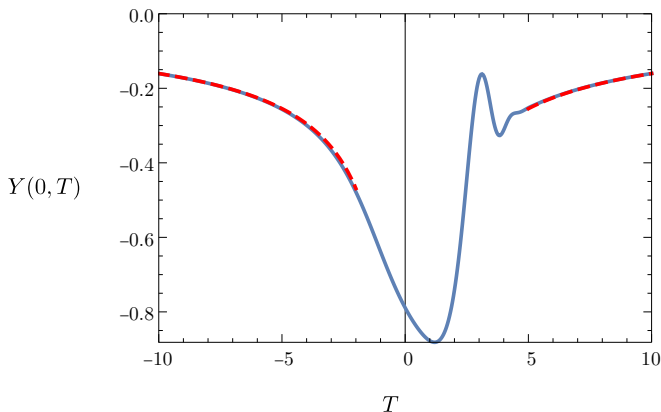


FIG. 14. Normalized free-surface displacement at the origin  $Y(0, T)$  versus normalized time  $T$ ; the large- $|T|$  behavior (34) is shown by the red dashed curves.

explains and quantifies the behavior observed in Fig. 9: The extremal response occurs when  $\ell f \sim 1$  and increases with both the amplitude  $A$  of the applied pressure and the sweeping amplitude  $\ell$ .

#### D. Higher-order resonances

In this section we explain the occurrence of the smaller local kinks and peaks in the response diagram of extremal displacement  $h$  versus frequency  $f$ , labeled I and II in Fig. 8.

The behavior of the solution  $h(x, t)$  in the  $(x, t)$  plane as the frequency is varied is shown in Fig. 15. Figures 15(a) and 15(b) show solutions at values of  $f$  that maximize the maximal film thickness and minimize the minimal film thickness, respectively. These both occur close to  $f = Q'(0)/\ell \approx 0.1$  here, in agreement with the traveling-wave analysis from Sec. VB. In particular, we observe in Fig. 15(b) a blue wave, corresponding to a local minimum in the film thickness, which appears to detach and propagate downstream from each inflection point in the pressure source locus. Again, this supports our hypothesis from Sec. VB that the minimum film thickness should occur when the translation velocity of the pressure source is stationary at the linear wave speed  $Q'(0) \approx 1$ .

Figure 15(c) shows the solution at the particular frequency marked I in Fig. 8. The maxima in  $h$  are indicated by the red contours in Fig. 15(c), and we observe that, at this critical frequency  $f_0 \approx 0.15$ , the locally maximal values of  $h$  upstream and downstream of the pressure source exactly coincide. Thus the slope discontinuity in the response diagram seen in Fig. 8 occurs when the location of the global supremal displacement switches, from the upstream maximum for  $f < f_0$  to the downstream maximum for  $f > f_0$ . This switch is illustrated more explicitly in Fig. 16, where we show several local extrema competing to be the global extremum as  $f$  is varied.

The local peak in the response marked II in Fig. 8 is caused by a global wave interaction. The corresponding solution in the  $(x, t)$  plane is shown in Fig. 15(d). Consider the blue wave, corresponding to a local minimum, shed from the pressure source close to its leftmost position  $x \approx -10$  at  $ft \approx 3\pi/2$ . This wave propagates downstream at the intrinsic wave speed  $Q'(0) \approx 1$  and interacts with the pressure source for a second time near its rightmost position  $x \approx 10$  at  $ft \approx 9\pi/2$ . What distinguishes this particular value of the frequency is that the blue wave is tangent to the locus of the pressure source twice and so benefits twice from the amplification effect discussed in Sec. VB, where the propagation speed and the intrinsic wave speed coincide.

This kind of long-range interaction can occur when a characteristic with speed  $dx/dt = Q'(0)$  is tangent to the sweeping profile  $x = \ell \sin(ft)$  at  $ft_1 = 3\pi/2 + \phi$  and again at  $ft_2 = (2n + 1/2)\pi - \phi$ , where  $\phi \in (0, \pi/2]$  and  $n$  is a positive integer. It is straightforward to show that  $\phi$

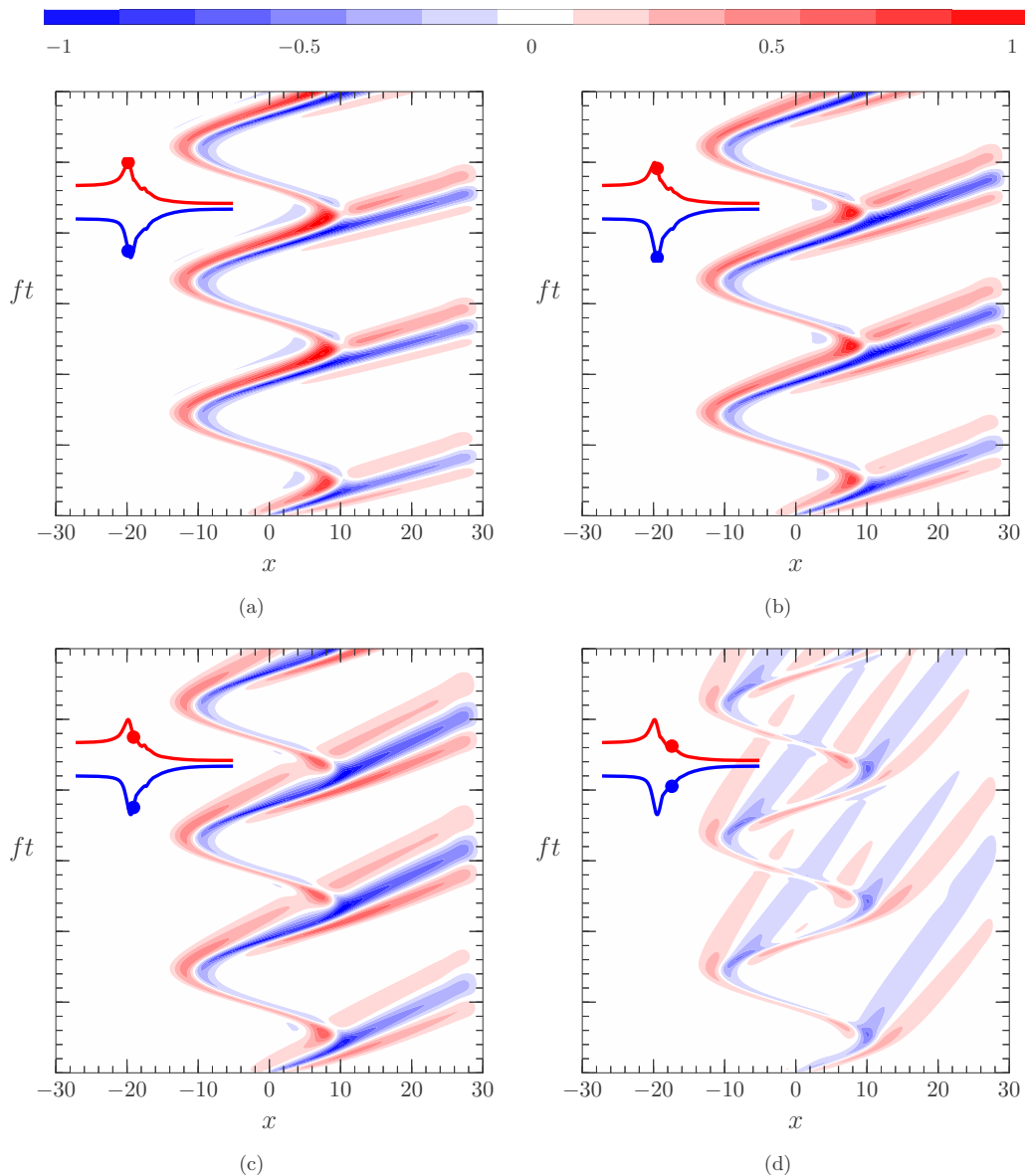


FIG. 15. Time-dependent solutions of (4) for the free-surface displacement  $h(x, t)$  with zero initial conditions and various values of the sweeping frequency parameter  $f$ , where  $A = 1$  and  $\beta = 0$ . The values of  $h$  in each case are indicated by the color bar at the top of the figure. The pressure, given by (5), is a sinusoidally moving Gaussian with  $\ell = 10$ . Each plot contains an inset duplicate of Fig. 8 with small disks marking the extrema for the corresponding value of  $f$ . Each solution was evolved until time  $t = 20/f$  and the time axis scaled to show the same number of oscillations in each case. The values of  $f$  were chosen to exhibit the special features of the response diagram in Fig. 8: (a)  $f = 0.095$ , the global maximum; (b)  $f = 0.12$ , the global minimum; (c)  $f = 0.15$ , the first gradient discontinuity; and (d)  $f = 0.45$ , the local peak due to wave interaction.

must satisfy the transcendental equation

$$\phi + \cot \phi = \left(n - \frac{1}{2}\right)\pi \quad (36)$$

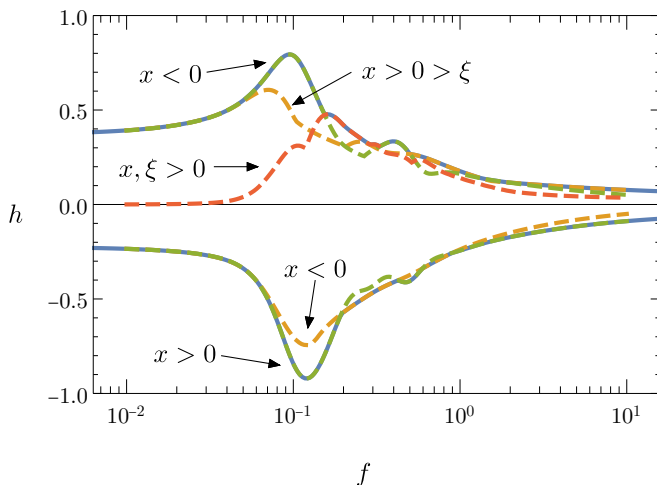


FIG. 16. Local and global minima of the free-surface displacement  $h$  plotted versus the sweeping frequency  $f$ , with  $A = 1$ ,  $\beta = 0$ , and  $\ell = 10$ . The dashed curves show local minima from regions upstream ( $x < 0$ ) and downstream ( $x > 0$ ) and local maxima from regions upstream ( $x < 0$ ), downstream beyond the center of the applied pressure ( $x, \xi > 0$ ), and downstream preceding the center of the applied pressure ( $x > 0 > \xi$ ). The underlying solid curves show the global extrema.

for an interaction where the pressure completes approximately  $2n - 1$  lengths of the sweeping region in time to coincide downstream with the deflection that it created upstream. The corresponding critical frequency is then given by

$$\ell f = Q'(0) \operatorname{cosec} \phi. \quad (37)$$

The first interaction mode  $n = 1$  gives  $\phi = \pi/2$  and  $\ell f = Q'(0)$ , which just reproduces the critical frequency for the principal response peak. The second mode  $n = 2$  gives  $\phi \approx 0.219$  and hence  $\ell f \approx 4.6Q'(0)$ , which is indeed close to the critical value of  $f$  identified in Fig. 15(d) when  $\ell = 10$  and  $Q'(0) \approx 1$ . In principle, higher-order interaction modes should occur when  $\ell f/Q'(0) \approx 7.79, 10.9, 14.1, \dots$ , but in practice the effect appears to be swamped by nonlinearity and damping, and we have been unable to discern any further local maxima in the response.

## VI. CONCLUSION

In this paper we considered the flow of a thin film of isothermal incompressible liquid driven by gravity down a substrate in the presence of a moving applied pressure. The problem exhibits two natural timescales: that characteristic of the motion of the applied pressure and that characteristic of the free surface deforming under the pressure. This allows us to consider three separate regimes: where the pressure moves on a timescale significantly slower or faster than the relaxation time and where these timescales are similar.

When the pressure moves slowly, the problem is quasisteady and the free-surface deflections are given by a steady-state profile that varies parametrically with time. When the pressure moves quickly, a formal multiple scales analysis shows that the momentum is spread along the length of the pressure oscillation. This results in the free surface deforming under an effective pressure given by the time-averaged pressure profile, which results in smaller pressure gradients and therefore causes smaller deflections than in the quasisteady case. When the pressure moves in the intermediate regime, the deflections can be significantly amplified. This large response is primarily caused by the pressure moving at a speed similar to the speed at which deflections of the free surface propagate downstream, so the pressure remains close to the trough it has created for a long time.

We used linearized models to quantify how the amplification of the free-surface response depends on the amplitude and frequency of the pressure oscillations. We demonstrated that the linear theory gives surprisingly good agreement with numerical solutions of the full nonlinear model for a wide range of parameter values. Nonetheless, it must be acknowledged that there are fundamental differences between the linear and nonlinear theories. The linear traveling-wave equation (23) admits bounded solutions that vanish in the far field for all values of  $L$  apart from the critical value  $L = 0$ , corresponding to  $V = Q'(0)$ , i.e., to the propagation speed being equal to the underlying characteristic wave speed. In contrast, as shown in [14], for example, the nonlinear version (22) in general exhibits nonexistence of solutions for a range of values of  $V$  close to  $Q'(0)$ . Our unsteady simulations, however, in principle allow us to find solutions for any parameter values, including those regions of parameter space where steady or traveling-wave solutions do not exist.

While the numerical simulations presented in this paper were for a particular magnetohydrodynamic flow, the phenomena described are generic and apply to magnetohydrodynamic flows with different field orientations, as well as the classical hydrodynamic case. It is for this reason that the Marangoni forcing in [16], although it is derived from a different mechanism entirely, results in a term analogous to the pressure gradient in our model and has a similar effect on the free surface.

There may be applications in which it is desirable to induce large resonant deflections. However, in the nuclear fusion context introduced here, the goal is to maintain a uniform coating of the substrate. In this case, the smallest possible deflections are desirable and are obtained by sweeping the pressure with high frequency and sufficiently large amplitude. If the system is unable to attain such high frequencies, then low frequencies should be used instead, to avoid the resonant range in which dangerous thinning of the film may occur.

In compliance with EPSRCs open access initiative, the data in this paper are available from Ref. [20].

#### ACKNOWLEDGMENTS

We would like to thank Dr. P. F. Buxton from Tokamak Energy for providing insight into confined fusion, to which we hope this research will contribute, as well as Professor J. C. R. Hunt, Professor J. R. Ockendon, and Dr. D. J. Allwright for engaging and helpful discussion on the problem. This paper was based on work supported by the EPSRC Centre For Doctoral Training in Industrially Focused Mathematical Modelling (Grant No. EP/L015803/1) in collaboration with Tokamak Energy.

#### APPENDIX: DERIVATION OF THE THIN-FILM MHD MODEL

In this Appendix we give a brief derivation of the thin-film equation (1) and the flux function (2) for thin-film Hartmann flow. We consider the two-dimensional geometry illustrated in Fig. 1, with velocity  $\mathbf{u}(x, y, t) = (u(x, y, t), v(x, y, t), 0)$ , where  $(x, y)$  are planar Cartesian coordinates parallel and normal to the fixed substrate at  $y = 0$ . Similarly, we consider a two-dimensional magnetic field  $\mathbf{B} = (B_x(x, y, t), B_y(x, y, t), 0)$ . It follows from Maxwell's equations that the electric field and the current must be purely in the  $z$  direction (out of the page in Fig. 1).

It is helpful to perform the decomposition

$$\mathbf{B} = \mathbf{B}^a + \mathbf{B}^i \tag{A1}$$

of the magnetic field  $\mathbf{B}$  into the *applied* field  $\mathbf{B}^a$  and the *induced* field  $\mathbf{B}^i$ . The applied field is imposed externally (in a tokamak by using an array of electromagnets) and therefore is assumed to be known and steady; moreover,  $\mathbf{B}^a$  must satisfy the free-space Maxwell equations  $\nabla \cdot \mathbf{B}^a = 0$  and  $\nabla \times \mathbf{B}^a = \mathbf{0}$ . We substitute (A1) into pre-Maxwell's equations (having negligible displacement currents) and Ohm's law for the magnetic field  $\mathbf{B}$ , electric field  $\mathbf{E}$ , and current in a liquid metal

flowing with velocity  $\mathbf{u}$  to obtain [17]

$$\nabla \cdot \mathbf{B}^i = 0, \quad \nabla \times \mathbf{B}^i = \mu \mathbf{j} = \mu \sigma (\mathbf{E} + \mathbf{u} \times \mathbf{B}), \quad \frac{\partial \mathbf{B}^i}{\partial t} = -\nabla \times \mathbf{E}, \quad (\text{A2})$$

where  $\sigma$  and  $\mu$  denote conductivity and magnetic permeability, respectively.

Now we use (A2) to estimate the magnitudes of the magnetic and electric fields induced by the flow of the liquid metal. Denoting by  $\mathcal{L}$ ,  $\mathcal{U}$ , and  $\mathcal{B}$  typical scales for the length, the velocity, and the applied magnetic field, we find that

$$\mathbf{B}^i \sim \text{Rm} \mathcal{B}, \quad \mathbf{E} \sim \text{Rm} \mathcal{U} \mathcal{B}, \quad (\text{A3})$$

where  $\text{Rm} = \mu \sigma \mathcal{U} \mathcal{L}$  is the so-called magnetic Reynolds number. Since  $\text{Rm}$  is invariably small for laboratory-scale liquid metal flows, we deduce that the induced magnetic field is small in comparison with the applied field. Thus (A2) reduces to

$$\nabla \cdot \mathbf{B} = 0, \quad \nabla \times \mathbf{B} = \mathbf{0}, \quad \mathbf{j} = \sigma \mathbf{u} \times \mathbf{B} \quad (\text{A4})$$

to lowest order in  $\text{Rm}$ , where  $\mathbf{B} \sim \mathbf{B}^a$  is now assumed to a known function of position. The velocity  $\mathbf{u}$  and pressure  $P$  in the fluid satisfy the incompressible Navier-Stokes equations with an additional Lorentz body force caused by the applied magnetic field, i.e.,

$$\nabla \cdot \mathbf{u} = 0, \quad (\text{A5a})$$

$$\rho \left( \frac{\partial \mathbf{u}}{\partial t} + (\mathbf{u} \cdot \nabla) \mathbf{u} \right) = -\nabla P + \rho \nu \nabla^2 \mathbf{u} + \rho \mathbf{g} + \mathbf{j} \times \mathbf{B}, \quad (\text{A5b})$$

where  $\rho$  and  $\nu$  are the density and the kinematic viscosity, respectively, and  $\mathbf{g} = g(\sin \theta, -\cos \theta, 0)$  is the acceleration due to gravity.

We impose the standard no-slip condition at the substrate, i.e.,

$$\mathbf{u} = \mathbf{0} \quad \text{at } y = 0. \quad (\text{A6})$$

At the free surface of the film, denoted by the graph  $y = H(x, t)$ , we impose the usual dynamic and kinematic boundary conditions, i.e.,

$$\begin{pmatrix} -P + 2\rho\nu \frac{\partial u}{\partial x} + p + \gamma \kappa & \rho\nu \left( \frac{\partial u}{\partial y} + \frac{\partial v}{\partial x} \right) - \tau \\ \rho\nu \left( \frac{\partial u}{\partial y} + \frac{\partial v}{\partial x} \right) - \tau & -P + 2\rho\nu \frac{\partial v}{\partial y} + p + \gamma \kappa \end{pmatrix} \begin{pmatrix} -\frac{\partial H}{\partial x} \\ 1 \end{pmatrix} = \mathbf{0} \quad \text{at } y = H(x, t), \quad (\text{A7a})$$

$$v = \frac{\partial H}{\partial t} + u \frac{\partial H}{\partial x} \quad \text{at } y = H(x, t), \quad (\text{A7b})$$

where  $p(x, t)$  and  $\tau(x, t)$  are the externally applied pressure and shear stress due to the plasma wind, respectively,  $\gamma$  is the surface tension, and  $\kappa(x, t)$  is the curvature of the free surface. In (A7a) we have neglected the contribution from the jump in the Maxwell stress, which is proportional to the magnetic susceptibility and therefore very small in the liquid metals of interest (of order  $10^{-5}$  for lithium, for example).

By integrating (A5a) with respect to  $y$  and imposing (A6) and (A7b), we obtain the exact conservation relation

$$\frac{\partial H}{\partial t} + \frac{\partial}{\partial x} \left( \int_0^H u \, dy \right) = 0. \quad (\text{A8})$$

Armed with this evolution equation for the free-surface height, we need not solve for  $v$ . Our aim is to use asymptotic analysis to approximate the horizontal velocity  $u$  and then substitute into (A8) to obtain an evolution equation for  $H(x, t)$ .

TABLE I. Dimensionless parameters, with the velocity and length scales defined by (A10). Typical parameter values for liquid lithium have been used [21,22],  $\mu = 1.3 \times 10^{-6}$  H/m,  $\sigma = 3 \times 10^6$  S/m,  $\nu = 10^{-6}$  m<sup>2</sup>/s,  $\gamma = 0.4$  N/m, and  $\rho = 500$  kg/m, along with a typical field strength  $\mathcal{B} = 1$  T, film height  $\mathcal{H} = 0.1$  mm, divertor inclination  $\theta = \pi/6$ , gravitational constant  $g = 9.8$  m/s<sup>2</sup>, and plasma pressure  $\mathcal{P} = 50$  Pa [23].

Dimensionless quantity	Definition	Typical value
aspect ratio	$\epsilon = \frac{\mathcal{H}}{\mathcal{L}}$	0.04
Reynolds number	$\text{Re} = \frac{\rho g \mathcal{L} \sin \theta}{\nu \sigma \mathcal{B}^2}$	2
magnetic Reynolds number	$\text{Rm} = \frac{\mu \rho g \mathcal{L} \sin \theta}{\mathcal{B}^2}$	$7.8 \times 10^{-6}$
Hartmann number	$\text{Ha} = \frac{\mathcal{B} \mathcal{H} \sqrt{\sigma}}{\sqrt{\rho \nu}}$	7.7
pressure amplitude	$A = \frac{\mathcal{P}}{\rho g \mathcal{L} \sin \theta} = \frac{\mathcal{P}}{(\gamma \mathcal{H})^{1/3} (\rho g \sin \theta)^{2/3}}$	8.3
transverse gravitational parameter	$\beta = \epsilon \cot \theta = \left( \frac{\rho g \mathcal{H}^2}{\gamma} \right)^{1/3} \frac{\cos \theta}{(\sin \theta)^{2/3}}$	0.07

We nondimensionalize via

$$x \mapsto \mathcal{L} x, \quad (\text{A9a})$$

$$u \mapsto \mathcal{U} u, \quad (\text{A9b})$$

$$P \mapsto (\rho g \mathcal{L} \sin \theta) P, \quad (\text{A9c})$$

$$p \mapsto \mathcal{P} p, \quad (\text{A9d})$$

$$H \mapsto \epsilon \mathcal{L} H, \quad (\text{A9e})$$

$$y \mapsto \epsilon \mathcal{L} y, \quad (\text{A9f})$$

$$v \mapsto \epsilon \mathcal{U} v, \quad (\text{A9g})$$

$$\mathbf{B} \mapsto \mathcal{B} \mathbf{B}, \quad (\text{A9h})$$

$$\tau \mapsto \mathcal{P} \tau, \quad (\text{A9i})$$

$$t \mapsto \frac{\mathcal{L}}{\mathcal{U}} t, \quad (\text{A9j})$$

where  $\epsilon = \mathcal{H}/\mathcal{L}$  is the small aspect ratio of the thin film and  $\mathcal{P}$  is the typical magnitude of the localized external stress profile. Suitable choices for the velocity and length scales, namely,

$$\mathcal{U} = \frac{\rho g \sin \theta}{\sigma \mathcal{B}^2}, \quad \mathcal{L} = \left( \frac{\gamma \mathcal{H}}{\rho g \sin \theta} \right)^{1/3}, \quad (\text{A10})$$

are found from dominant balances in (A5b) and (A7a). With this choice of length scale, the aspect ratio is given by  $\epsilon = (\rho g \mathcal{H}^2 \sin \theta / \gamma)^{1/3}$ , i.e. the cube root of the Bond number.

Substitution of (A9) into the governing equations and boundary conditions (A4)–(A7) produces a number of dimensionless parameters, which are listed in Table I. We neglect small terms of order  $\epsilon$ ,  $\epsilon^2 \text{Re}$ , and  $\text{Rm}$  to obtain the leading-order lubrication equations

$$\frac{\partial P}{\partial x} = \frac{1}{\text{Ha}^2} \frac{\partial^2 u}{\partial y^2} + 1 - u B(x)^2, \quad (\text{A11a})$$

$$\frac{\partial P}{\partial y} = -\beta, \quad (\text{A11b})$$

where  $B(x) = B_y^a(x, 0)$  defines the dimensionless vertical component of the applied magnetic field evaluated on the divertor. The corresponding boundary conditions are

$$u = 0 \quad \text{at } y = 0, \quad (\text{A11c})$$

$$P = Ap - \frac{\partial^2 H}{\partial x^2} \quad \text{at } y = H(x, t), \quad (\text{A11d})$$

$$\frac{\partial u}{\partial y} = 0 \quad \text{at } y = H(x, t). \quad (\text{A11e})$$

Here we retain the apparently small term of order  $1/\text{Ha}^2$  in (A11a), since the problem (A11) is singular in the limit  $\text{Ha} \rightarrow \infty$ . In this paper we are mainly interested in situations where the inclination angle  $\theta$  is  $O(1)$  so that the flow is driven principally by the downslope component of gravity. Nevertheless, for the moment, we also retain in (A11b) the transverse gravitational term  $\beta = \epsilon \cot \theta$ , which might be non-negligible in cases where  $\theta$  is  $O(\epsilon)$ .

By integrating (A11b) and imposing (A11d), we obtain the leading-order pressure

$$P = Ap + \beta(H - y) - \frac{\partial^2 H}{\partial x^2}. \quad (\text{A12})$$

Substitution of (A12) into (A11a) gives an equation for  $u$ , namely,

$$\frac{1}{\text{Ha}^2} \frac{\partial^2 u}{\partial y^2} - uB^2 + C(x, t) = 0, \quad (\text{A13a})$$

where

$$C(x, t) = 1 - A \frac{\partial p}{\partial x} - \beta \frac{\partial H}{\partial x} + \frac{\partial^3 H}{\partial x^3}. \quad (\text{A13b})$$

Equation (A13), along with boundary conditions (A11c) and (A11d), has the solution

$$u(x, y, t) = \frac{C(x, t)}{B(x)^2} \left[ 1 - \frac{\cosh\{\text{Ha } B(x)[H(x, t) - y]\}}{\cosh[\text{Ha } B(x)H(x, t)]} \right]. \quad (\text{A14})$$

By substituting (A14) into (A8), we obtain the equation governing the evolution of the free surface, namely,

$$\frac{\partial H}{\partial t} + \frac{\partial}{\partial x} \left[ q(H; x) \left( 1 - A \frac{\partial p}{\partial x} - \beta \frac{\partial H}{\partial x} + \frac{\partial^3 H}{\partial x^3} \right) \right] = 0, \quad (\text{A15})$$

where

$$q(H; x) = \frac{H}{B(x)^2} \left[ 1 - \frac{\tanh[\text{Ha } B(x)H]}{\text{Ha } B(x)H} \right]. \quad (\text{A16})$$

Since the external magnetic field  $B$  varies on the length scale of the entire divertor, which is of order  $1 \text{ m} \gg \mathcal{L}$ , we expect  $B$  to be approximately constant (and equal to 1 by our choice of nondimensionalization) over the range of values of  $x$  relevant in this paper. Therefore, (A15) and (A16) reduce to (1), with  $q$  given by (2).

In the limit  $\text{Ha} \rightarrow 0$ , corresponding to a weak applied magnetic field, the velocity (A14) reduces to the classical quadratic profile

$$u|_{\text{Ha} \ll 1} = \frac{\text{Ha}^2 C}{2} y(2H - y). \quad (\text{A17})$$

The corresponding flux function  $q = \text{Ha}^2 H^3/3$  is independent of  $B$  and varies cubically with  $H$ . In the opposite limit  $\text{Ha} \rightarrow \infty$ , relevant to the strong magnetic fields found in a divertor, the horizontal

velocity profile is approximately uniform outside a boundary layer at  $y = 0$ , typical of Hartmann flow, and is given by

$$u|_{\text{Ha} \gg 1} = \frac{C}{B^2}. \quad (\text{A18})$$

In this limit, the flux function is given by  $q = H/B(x)^2$ . In general, the flux  $q$  is a decreasing function of  $|B|$ : The larger the  $y$  component of the applied field, the slower the horizontal velocity, as the magnetic forces retard the flow.

- 
- [1] R. V. Craster and O. K. Matar, Dynamics and stability of thin liquid films, *Rev. Mod. Phys.* **81**, 1131 (2009).
- [2] A. Oron, S. H. Davis, and S. G. Bankoff, Long-scale evolution of thin liquid films, *Rev. Mod. Phys.* **69**, 931 (1997).
- [3] T. G. Myers, Thin films with high surface tension, *SIAM Rev.* **40**, 441 (1998).
- [4] P. Fifiis, M. Christenson, M. Szott, K. Kalathiparambil, and D. N. Ruzic, Free surface stability of liquid metal plasma facing components, *Nucl. Fusion* **56**, 106020 (2016).
- [5] M. Ono, R. Majeski, M. A. Jaworski, Y. Hirooka, R. Kaita, T. K. Gray, R. Maingi, C. H. Skinner, M. Christenson, and D. N. Ruzic, Liquid lithium loop system to solve challenging technology issues for fusion power plant, *Nucl. Fusion* **57**, 116056 (2017).
- [6] M. Wischmeier, Simulating divertor detachment in the TCV and JET tokamaks, Ph.D. thesis, École Polytechnique Fédérale de Lausanne, 2005.
- [7] L. J. Haworth and L. D. P. King, The stopping power of lithium for low energy protons, *Phys. Rev.* **54**, 48 (1938).
- [8] G. V. Miloshevsky and A. Hassanein, Modelling of Kelvin-Helmholtz instability and splashing of melt layers from plasma-facing components in tokamaks under plasma impact, *Nucl. Fusion* **50**, 115005 (2010).
- [9] M. A. Jaworski, T. Abrams, J. P. Allain, M. G. Bell, R. E. Bell, A. Diallo, T. K. Gray, S. P. Gerhardt, R. Kaita, H. W. Kugel, B. P. LeBlanc, R. Maingi, A. G. McLean, J. Menard, R. Nygren, M. Ono, M. Podesta, A. L. Roquemore, S. A. Sabbagh, F. Scotti, C. H. Skinner, V. A. Soukhanovskii, D. P. Stotler, and the NSTX Team, Liquid lithium divertor characteristics and plasma-material interactions in NSTX high-performance plasmas, *Nucl. Fusion* **53**, 083032 (2013).
- [10] G. A. Mesyats and N. M. Zubarev, The Rayleigh-Plateau instability and jet formation during the extrusion of liquid metal from craters in a vacuum arc cathode spot, *J. Appl. Phys.* **117**, 043302 (2015).
- [11] J. T. Holgate, M. Coppins, and J. E. Allen, Electrohydrodynamic stability of a plasma-liquid interface, *Appl. Phys. Lett.* **112**, 024101 (2018).
- [12] Y. Shi, G. Miloshevsky, and A. Hassanein, Boiling induced macroscopic erosion of plasma facing components in fusion devices, *Fusion Eng. Des.* **86**, 155 (2011).
- [13] E. O. Tuck and J.-M. Vanden Broeck, Influence of surface tension on jet-stripped continuous coating of sheet materials, *AIChE J.* **30**, 808 (1984).
- [14] J. J. Kriegsmann, M. J. Miksis, and J.-M. Vanden Broeck, Pressure driven disturbances on a thin viscous film, *Phys. Fluids* **10**, 1249 (1998).
- [15] J. Quintans Carou, S. K. Wilson, N. J. Mottram, and B. R. Duffy, Asymptotic and numerical analysis of a simple model for blade coating, *J. Eng. Math.* **63**, 155 (2008).
- [16] R. P. Haskett, T. P. Witelski, and J. Sur, Localized Marangoni forcing in driven thin films, *Physica D* **209**, 117 (2005).
- [17] P. H. Roberts, *An Introduction to Magnetohydrodynamics* (Elsevier, New York, 1967).
- [18] L. Zhornitskaya and A. L. Bertozzi, Positivity-preserving numerical schemes for lubrication-type equations, *SIAM J. Numer. Anal.* **37**, 523 (1999).

- [19] See Supplemental Material at <http://link.aps.org/supplemental/10.1103/PhysRevFluids.3.114801> for movies.
- [20] <http://dx.doi.org/10.5287/bodleian:wx1PG9J4P>.
- [21] H. W. Davison, Compilation of thermophysical properties of liquid lithium, NASA Report No. TN D-4650, 1968 (unpublished).
- [22] K. Shimokawa, T. Itami, and M. Shimoji, On the temperature dependence of the magnetic susceptibility of liquid alkali metals, *J. Phys. F* **16**, 1811 (1986).
- [23] N. B. Morley, A. A. Gaizer, and M. A. Abdou, Estimates of the effect of a plasma momentum flux on the free surface of a thin film of liquid metal, *Fusion Eng. Des.* **28**, 176 (1995).